Transition and Instability Measurements in a Mach 6 Hypersonic Quiet Wind Tunnel

Brandon C. Chynoweth,* Christopher A. C. Ward,* Ryan O. Henderson,* C. George Moraru,*
Roger T. Greenwood,† Andrew D. Abney,* and Steven P. Schneider‡

School of Aeronautics and Astronautics

Purdue University

West Lafayette, IN 47907-1282

This paper details five different projects in the Boeing/AFOSR Mach 6 Quiet Tunnel (BAM6QT) at Purdue University. In the first project, a highly swept fin on a 7° half-angle cone was examined. Temperature sensitive paint and pressure fluctuation measurements showed the presence of an instability near 200 kHz. In the second, the effect of roughness on the stationary and travelling crossflow instabilities was investigated on a cone at an angle of attack. It was found that when the roughness generated larger stationary waves, the travelling waves were damped. In the third, discrete roughness elements made of epoxy were applied to a flared cone. The roughness elements were sized to interact with the second-mode waves without becoming a trip. Using this technique, the spacing of streaks of increased heating was controlled. The fourth project involves improving the current pulsed jet perturber used to study nozzle-wall boundary-layer perturbations. Two improvements have been designed and have undergone preliminary testing. Finally, a new model was designed to measure what appears to be an entropy-layer instability at Mach 6. Surface pressure measurements and hot-wire data are used to investigate the entropy layer.

I. Introduction

A. Hypersonic Laminar-Turbulent Transition

Boundary-layer transition at hypersonic speeds is a process that is difficult to predict. Hypersonic laminar-turbulent transition affects heat transfer, skin friction, separation, and other boundary-layer properties. Therefore, it is important that accurate methods of prediction and control of transition be developed to ensure that flight vehicles are not over-designed. If a hypersonic vehicle is designed to withstand a worst-case scenario, it may have excessive heat shielding. The additional weight of heavy shielding materials would cause the vehicle to suffer from reduced maneuverability and range.

Conventional hypersonic tunnels have noise levels between 1-4%. This noise level can be more than an order of magnitude larger than noise levels at actual flight conditions and cause transition to occur earlier than in quiet flow. Quiet wind tunnels are designed to have freestream noise levels that are significantly lower than conventional tunnel. With freestream noise levels of 0.1% or less, quiet wind tunnels provide test conditions that can be used to study laminar-turbulent transition at noise levels similar to flight.

---

*Research Assistant. Student Member, AIAA
†Research Assistant. Senior Member, AIAA
‡Professor. Associate Fellow, AIAA

B.   The Boeing/AFOSR Mach-6 Quiet Tunnel

The Boeing/AFOSR Mach-6 Quiet Tunnel (BAM6QT) is the larger of two hypersonic quiet wind tunnels in the United States at present. The BAM6QT is a Ludweig tube design incorporating a long driver tube with a converging-diverging nozzle at the downstream end. A schematic of the tunnel is shown in Figure 1. In order to operate the tunnel, a pair of diaphragms downstream of the test section are burst causing an expansion fan to propagate upstream through the test section and driver tube. The air behind the expansion fan is accelerated through the nozzle to create Mach 6 flow in the test section.
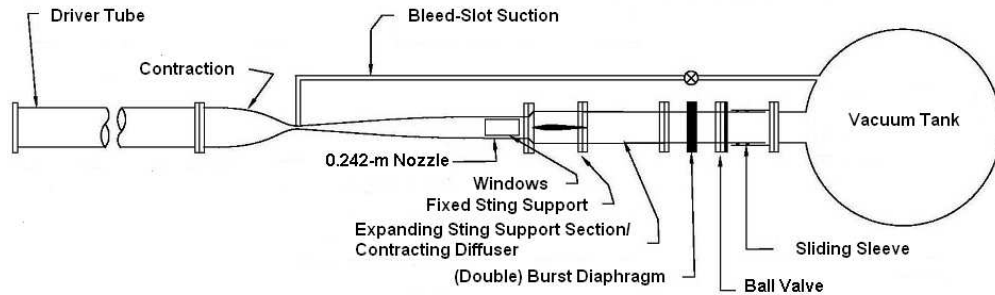

Figure 1. Schematic of Boeing/AFOSR Mach 6 Quiet Tunnel.

Using several unique features, the BAM6QT is able to produce noise levels on the order of 0.05%. A suction slot upstream of the throat is connected to the vacuum tank and can be used to remove the boundary layer on the nozzle wall. This allows for a fresh laminar boundary layer to grow on the nozzle wall starting near the throat. If the operator chooses not to use the suction slot, the tunnel can be operated with noise levels of the order of 3%, similar to conventional hypersonic facilities. The long divergent portion of the nozzle was designed to minimize the growth of Görtler instabilities and is polished to a mirror finish. Additionally, to reduce the risk of particulate matter scratching the mirror finish, 1 micron air filters are used to remove particles in the air used to pressurize the driver tube.

II.   7° Half-Angle Cone with a Highly Swept Fin

Three fin geometries with varying leading edge angles were designed and tested on a 7° half-angle circular cone at 0° angle of attack. Heat transfer characteristics affected by corner flow were quantitatively obtained using temperature sensitive paint and a Schmidt-Boelter (SB) gauge. Additionally, the formation of an instability for the varying fin geometries was studied using PCB fast-pressure sensors.

A.   Model

The cone (Figure 2) has two parts, a frustrum and a nosetip, both of which are constructed from 6061-T6 aluminum. The cone is 40.6 cm long with a base diameter of 10.0 cm.

Three fin geometries were designed with leading edge angles of 5°, 7.5°, and 10°. The three fins are shown in Figure 3. The fins were symmetrically tapered to a sharp leading edge. All three geometries were constructed from 6061-T6 aluminum. The 5° and 10° fins have a length of 25.4 cm while the 7.5° fin has a length of 25.0 cm due to manufacturing difficulties. All fins have a maximum height above the cone surface of 2.2 cm.

B.   Heat Transfer Results

Temperature sensitive paint results show three regions of increased heating; the leading edge of the fin, an axial streak along the fin, and an axial streak down the surface of the cone. Increased heat flux seen at

2

Figure 2. 7° half-angle cone with temperature sensitive paint applied and no fin installed.
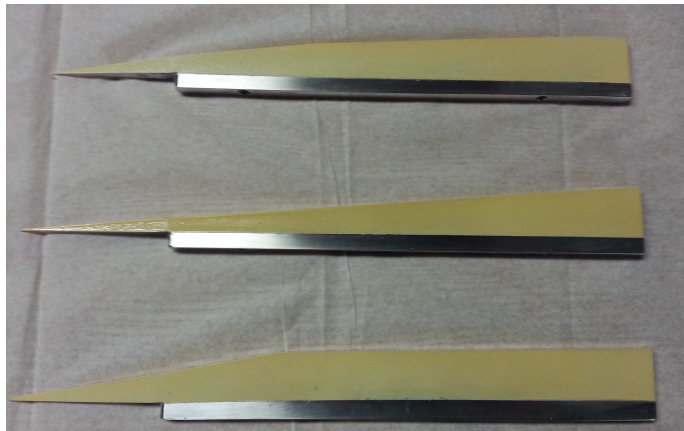

Figure 3. 7.5°, 5°, and 10° fins, from top to bottom.

the leading edge of the fin is expected due to the local temperature increase caused by the oblique shock from the leading edge. Previous experiments on corner flows[1] showed that the axial streak of increased heat transfer along the fin was induced by a vortical structure. The axial streak down the cone is believed to be created by the shock formed from the leading edge of the fin.

Figure 4 shows the leading edge of the fin, the vortical structure and the shock along the cone. As the leading edge angle was increased, all regions of interest had increases in heat transfer.
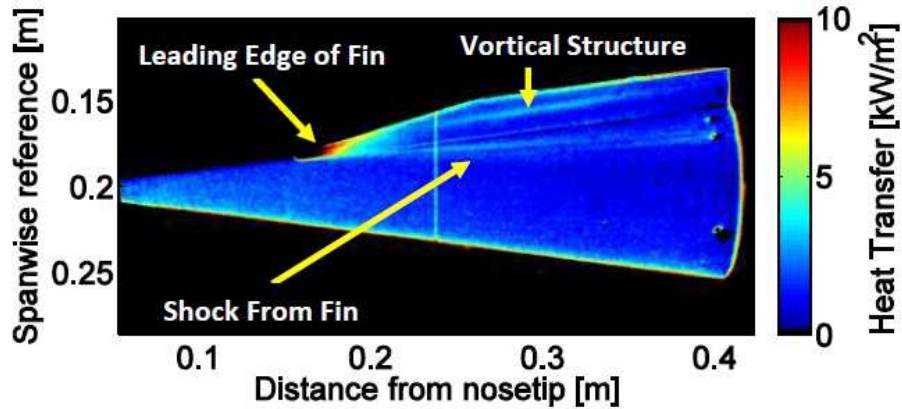

Figure 4. Global heat flux for 10° fin at Re = 9.68×10⁶/m, p_0 = 134 psia, T_0 = 437 K.

A range of Reynolds numbers were also tested throughout the experiment. Two runs for the 7.5° fin are compared in Figure 5(a) and 5(b). With an increase in unit Reynolds number, the heat transfer is increased at the leading edge, vortical structure, and shock from the fin. The heat flux at the leading edge of both figures is greater than $10\frac{kW}{m^2}$ and is colored in black. The same results were found for the 5° and 10° fins.

C. Pressure Measurements

Three PCB-132 fast-pressure sensors were installed in the model to measure pressure fluctuations. Figure 6 shows the approximate location of each sensor. All sensors are axially 29.97 centimeters downstream of the nosetip. Using results from TSP testing, a PCB was placed inside the location where the shock appeared to impinge on the surface of the cone. This PCB location will be referred to as Inside Shock. Again using TSP results, the original location of the SB gauge was observed to be near the shock. Therefore, results from the PCB at this location will be referred to as Near Shock. Finally, a PCB was placed at an angular distance of 90 degrees from the centerline of the fin. This sensor will be referred to as the PCB Outside Shock.

1. Inside Shock Results

At quiet conditions, neither the variation of fin angle nor the unit Reynolds number affected the pressure fluctuations behind the shock. Slight differences do become apparent when the fins are tested under noisy conditions. At approximately 290 kHz and 310 kHz, a peak in the power spectral density occurs for all three fins as shown in Figure 7 for the 10° fin. The cause of these peaks was not determined.

2. Near Shock Results

Under quiet conditions, one primary pressure fluctuation is observed when testing the 5° and 7.5° fins. The fluctuation is first observed at a frequency of approximately 175 kHz and increases in frequency by 10 percent as the unit Reynolds number increases by nearly 25 percent as seen in Figure 8. The instability has similar frequencies as a second mode wave on this model, but has not been confirmed as such. Using TSP imaging,

4
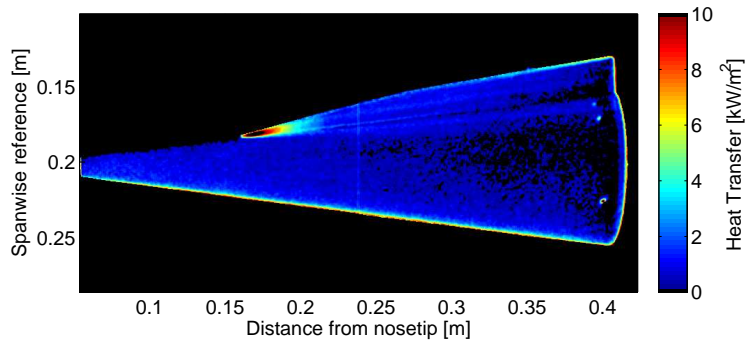
(a) 7.5° fin at $\mathrm{Re} = 7.93 \times 10^6/\mathrm{m}$, $p_0 = 106$ psia, $T_0 = 428$ K.
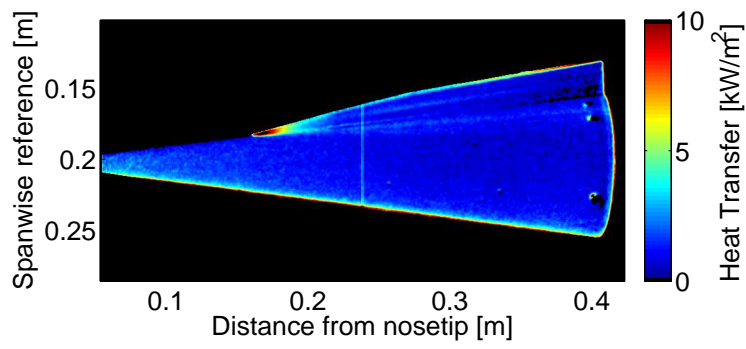
(b) 7.5° fin at $\mathrm{Re} = 9.97 \times 10^6/\mathrm{m}$, $p_0 = 135$ psia, $T_0 = 428$ K.

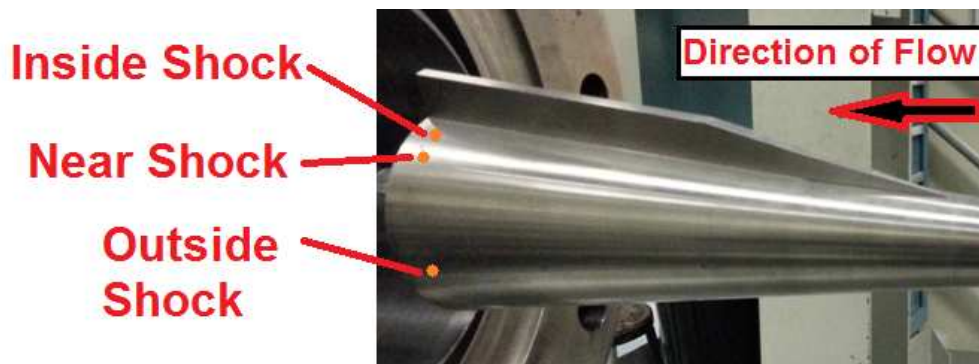**Figure 5. Global heat flux at minimum and maximum unit Reynolds numbers tested.**

Figure 6. Approximate location of PCB-132 sensors on fin-cone model.
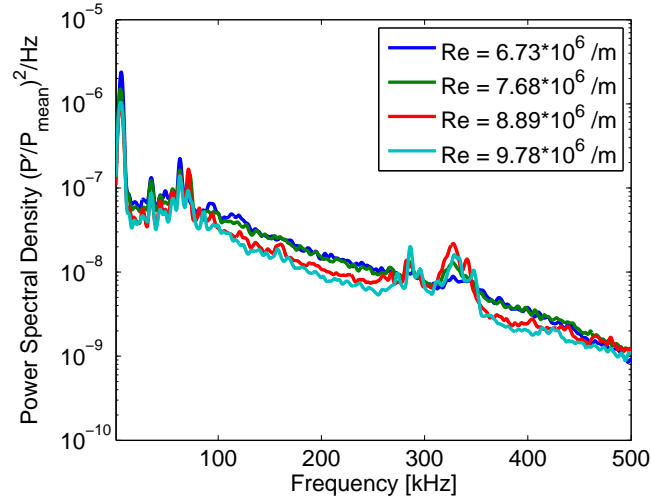
5

Figure 7. Power spectral density of pressure fluctuations inside shock with a 10° fin with noisy flow.

it could be seen that the location of this PCB is just upstream of the location of peak heating on the surface of the cone.
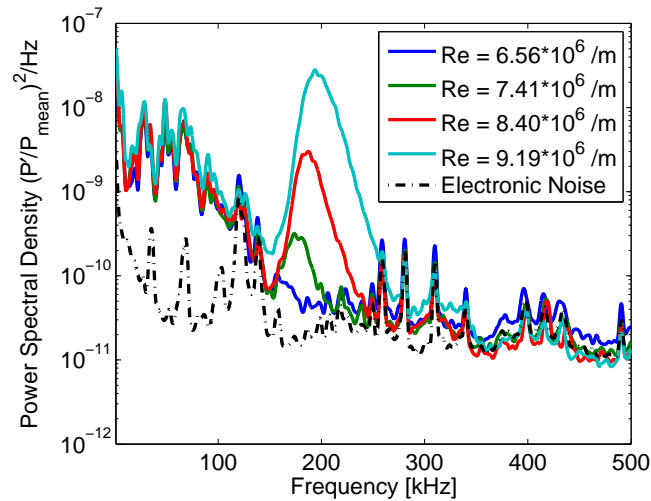

Figure 8. Power spectral density of pressure fluctuations near shock with a 5° fin with quiet flow.

For the 10° fin, as the unit Reynolds number increases a peak near 200 kHz increases in frequency. Continuing to increase the unit Reynolds number, the broadband noise of the spectrum increases and a distinct peak is no longer observed as shown in Figure 9. The flow may have become turbulent. Since the broadband increase in noise was not seen at similar unit Reynolds numbers for the other fins, the spectra is assumed to be the result of altering the fin geometry. The exact cause was not determined and requires further testing.
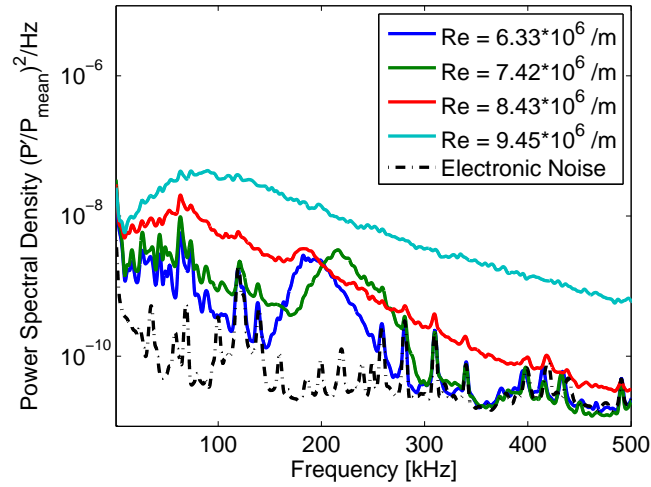
6

Figure 9. Power spectral density of pressure fluctuations near shock with a 10° fin with quiet flow.

3. *Results Outside Shock*

Under noisy flow, a peak centered at 200 kHz, most likely the second mode instability, was observed for all three fins at the lowest unit Reynolds number tested. As the unit Reynolds number increased, the peak decreased in magnitude as seen in Figure 10. The overall increased broadband noise suggests that the flow is intermittent for all unit Reynolds numbers tested. As the unit Reynolds number increases, the continued transition towards turbulence leads to the breakdown of second mode waves. Casper[2] observed the breakdown of second mode waves on a 7° cone at similar unit Reynolds numbers in the BAM6QT under noisy flow. Usually, the breakdown will cause peaks in the power spectral density at harmonic frequencies of the initial instability. Since it is believed that the flow is intermittent with a raised noise floor at all Reynolds numbers tested, these additional peaks are not observed as the second mode waves break down.
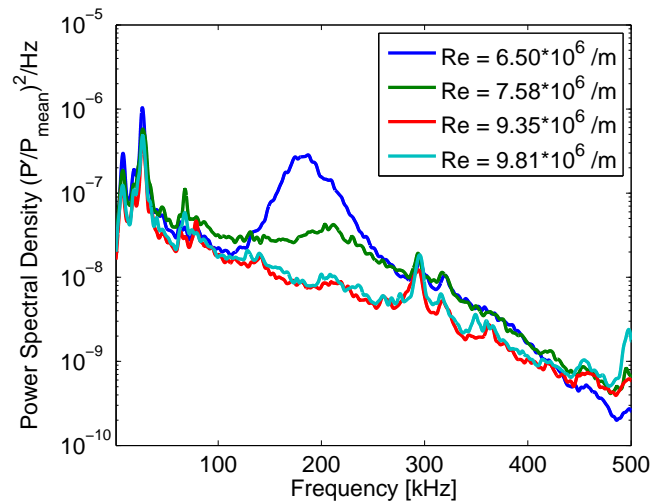

Figure 10. Power spectral density of pressure fluctuations 90° from windward from a 7.5° fin with noisy flow.

7

III.   Crossflow Instability and Transition on a Cone at Angle of Attack

There are several instabilities that can cause transition in a three-dimensional boundary layer, including the centrifugal, streamwise, and crossflow instabilities. For an axisymmetric cone in hypersonic flow pitched at an angle of attack, a circumferential pressure gradient is created due to a stronger shock near the windward ray. The circumferential pressure gradient causes the inviscid streamlines to be curved. In the boundary layer, there is an imbalance between the pressure gradient and the centripetal acceleration because the streamwise velocity is reduced, but the pressure gradient does not change. This imbalance causes a secondary flow (crossflow) in the boundary layer perpendicular to the inviscid streamlines. Crossflow must vanish at the wall and the edge of the boundary layer, creating an inflection point in the crossflow velocity profile.[3] Crossflow is thus inviscidly unstable and manifests as co-rotating vortices centered around the inflection point. Crossflow waves can be either travelling or stationary with respect to the surface. It has been verified experimentally for low speeds that the stationary waves tend to dominate in low-disturbance environments such as in flight or in low-noise tunnels, while the travelling waves tend to dominate in high-disturbance environments such as conventional tunnels.[4]

The stationary waves appear to be sensitive to small roughness placed near the wave's neutral point. Both Saric (at low speeds) and Corke (at high speeds) have had much success in using discrete roughness elements to control the stationary vortices.[3,5–7] Depending on the spacing of the roughness, certain stationary vortex wavelengths could be forced, and crossflow-induced transition could be delayed. A very limited amount of work has studied the interaction (if any) between the travelling and stationary waves. Preliminary work by Borg[8] showed that depending on the spacing of discrete roughness elements on an elliptical cone at Mach 6, the travelling waves could be damped.

A.   Effect of Roughness on Stationary and Travelling Waves

Experiments were performed in September 2013 to obtain global heat transfer and pressure fluctuations on a 7° half-angle cone at 6° angle of attack. A more detailed description of the heat-transfer calibration method is given in Reference 9. Pressure measurements were obtained using an array of Kulite fast pressure transducers. Roughness was added to the cone via nail polish as shown in Figure 11, or by a rough paint finish. Three sets of tests were done; one with a smooth paint finish, one with a patch of rough paint, and one with two patches of rough nail polish. The smooth paint had an RMS roughness of 0.37 μm. The downstream nail polish patch had an RMS roughness of 0.90 μm, an axial location of 23.5 cm and spanned from approximately 80–100° azimuthally. The upstream nail polish patch had an RMS roughness of 3.1 μm, an axial location of 19.2 cm and spanned from approximately 60–100° azimuthally. The rough paint patch was not characterized before removing via sanding. Figure 11 also shows the location of the Kulite pressure transducer array. The Kulite array was fixed at an azimuthal angle of approximately 90° from the windward ray.
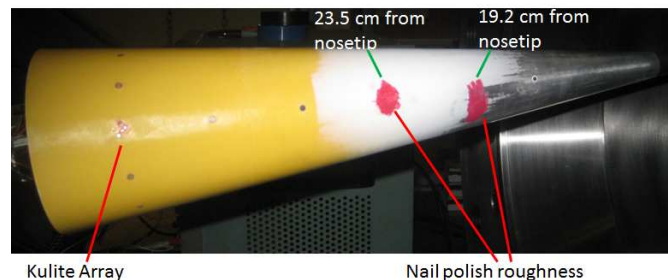

Figure 11.   7° half angle cone with Kulite array and nail polish roughness patches.

The three sets of tests were performed under quiet flow at a unit Reynolds number of approximately 10×10^6/m. The TSP images for the tests are shown in Figure 12. Comparing the smooth wall to the rough

paint patch, it is clear that the rough paint is generating larger stationary waves. The case with the nail polish roughness also shows stationary waves with a slightly larger magnitude as compared to the smooth case. This becomes more clear in Figure 13. Figure 13 plots spanwise heat transfer profiles (normalized by the mean heat transfer) of the TSP images in Figure 12, at an axial location of 0.35 m. Once again, the nail polish roughness and rough paint cases are producing larger magnitude stationary waves compared to the smooth paint case, with the rough paint case producing the largest stationary waves. The Kulite array is near the spanwise reference of 0 m.

Travelling crossflow waves were measured using the Kulite pressure transducer array. Figure 14 plots the power spectral density of one Kulite in the array at an azimuthal angle of 90° for each of the three cases. The smooth case shows a peak at approximately 40 kHz, which appears to be the travelling crossflow waves. When the roughness is added to the cone and the magnitude of the stationary waves increases, the magnitude of the travelling waves decreases as in Borg.[8] The nature of this travelling and stationary wave interaction may be significant, but is poorly understood. Much more work is required to better understand this phenomenon.

B. Effect of Wall Temperature on Travelling Waves

Borg looked at the repeatability of travelling wave measurements on an elliptical cone in the BAM6QT.[8] It was found that the measured peak frequency agreed from run to run, but the amplitude of the waves did not. The amplitudes were found to vary by up to an order of magnitude. It was hypothesized that the amplitudes of the waves were being affected by the increasing model temperature throughout the course of a day, because after each run the model temperature increases due to convection. The model temperature was not measured so therefore this hypothesis could not be confirmed.

Five consecutive runs were performed at approximately the same unit Reynolds number of 10.0×10^6/m by the present author. For the first four runs, the runs were performed as quickly as possible, allowing the model to heat up as much as possible. The fifth run was performed after allowing the model to cool down for several hours. Figure 15 plots the power spectral density of a Kulite pressure transducer 0.36 m axially from the nosetip and at an azimuthal angle of 110° from the windward ray for the five runs.

For all five runs, the spectra show approximately the same travelling-crossflow peak frequency near 40 kHz. As the wall temperature increases, the amplitude of the wave increases. Comparing runs 29 and 32, the wall temperature increases by about 3.6% and the amplitude increases by a factor of approximately 2.5. This increase in amplitude is not as significant as the order of magnitude change Borg measured. Run 33, which was performed after allowing the model to cool down, shows a similar amplitude to Run 30 and both have similar wall temperatures. Thus, the travelling waves seem to be very sensitive to small changes in the model wall temperature.

IV.   Transition and Instabilities Measurements on a Flared Cone

### A.   Brief Background and Previous Experiments

The flared cone was designed to study the non-linear transition process in a hypersonic boundary layer. The shape of the cone maintains a constant-thickness boundary layer. Since the frequency of the second mode wave is dominated by boundary layer thickness, large amplitude waves can be measured over a narrow frequency band. Using TSP images, the transition process can be observed experimentally. Streaks of increased temperature occur on the cone followed by a decrease to near laminar levels. If the Reynolds number is large enough, a second increase in heating is observed. This second increase in heating is due to the flow transitioning to turbulence as has been verified using pressure fluctuation measurements.[9] The goal of current work is to control the streaks through the use of discrete roughness elements. Chou first used nail polish dots to alter the second-mode waves. The results showed that discrete roughness elements could affect the streaks, but the nail polish proved difficult to apply in a consistent manner.[11] Luersen tested several methods including rub-on dots, metallic wafer inserts, and epoxy dots applied with an electronic fluid dispensing device. The epoxy dots could be applied in the most consistent manner. The epoxy dots that
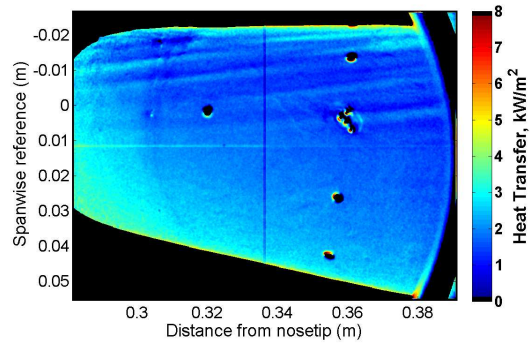
(a) Smooth paint. $p_0 = 140.6$ psia, Re $= 11.5 \times 10^6$/m, $T_0 = 423$ K, $T_{wall} = 298$ K
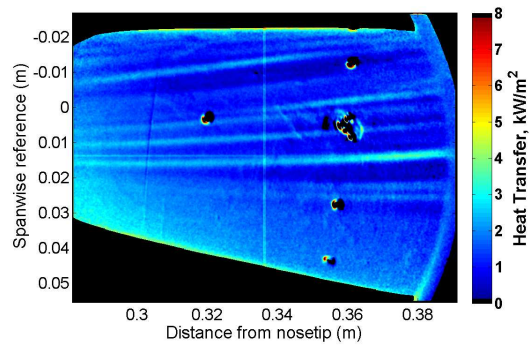
(b) Rough paint patch. $p_0 = 139.8$ psia, Re $= 11.1 \times 10^6$/m, $T_0 = 430$ K, $T_{wall} = 299$ K
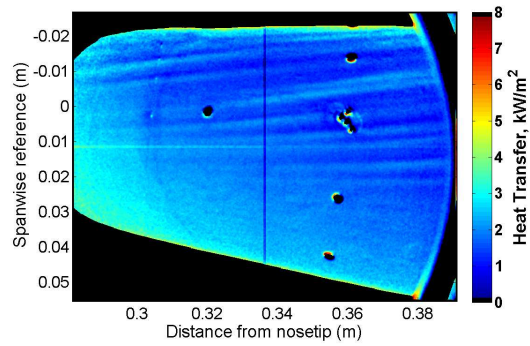
(c) Nail polish roughness. $p_0 = 139.1$ psia, Re $= 11.5 \times 10^6$/m, $T_0 = 421$ K, $T_{wall} = 299$ K

Figure 12. TSP images of the 7° half-angle cone at 6° angle of attack under quiet flow. Yaw side of the cone.
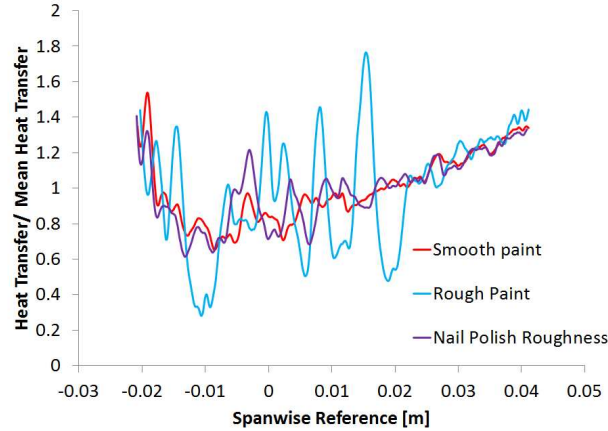
Figure 13. Spanwise heat-transfer profiles at an axial distance of 0.35 m from the TSP images in Fig. 12. Kulite pressure transducer array located at a spanwise reference value of 0 m.
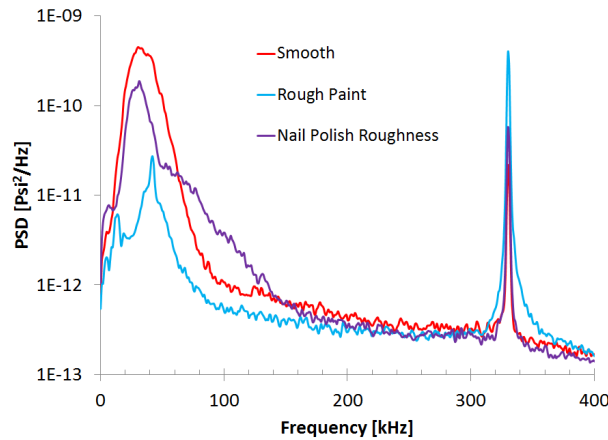

Figure 14. Power spectral density of surface pressure at an axial distance 0.36 m and an azimuthal angle of 90°.

Luersen produced were either too small to have an effect on the streaks, or they were too large and caused the flow to transition without interacting with the second-mode waves.[9, 12]

B. Current Results

The electronic fluid dispensing device was again used to apply epoxy dots to the surface of the cone. All roughness elements were applied 17.4 cm from the tip of the model. Thirty epoxy dots were applied in 12° increments. An iterative approach was used to determine the height of the roughness element that interacted with the second-mode waves without becoming a boundary layer trip under quiet tunnel conditions. Figure 16 shows a typical TSP image of the flared cone without any roughness elements at a unit Reynolds number of 10.9×10^6/m. The wave number around the circumference of the frustum is approximately 80. Using PCB 132A31 fast pressure transducers, it was determined that the second-mode wave of maximum amplitude had a frequency centered at 315 kHz. The asymmetry seen in the TSP image shows the sensitive nature of second-mode waves. This sloping of the initial increase in heating around the cone could be caused by temperature gradients in the freestream or a slight misalignment of the model with the freestream flow.
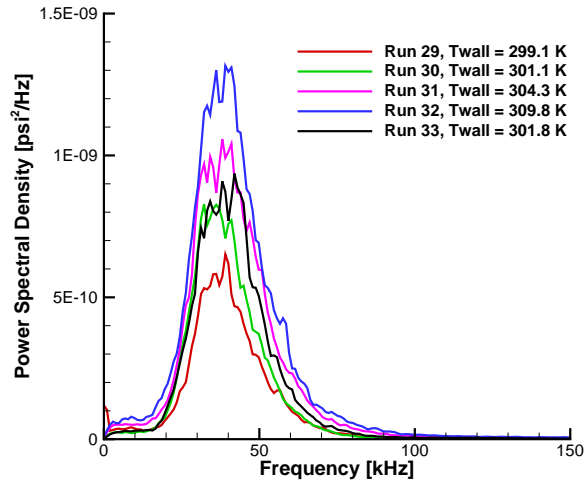
11

Figure 15. Power spectral density of surface pressure at an axial distance 0.36 m and an azimuthal angle of 110° with varying wall temperatures.
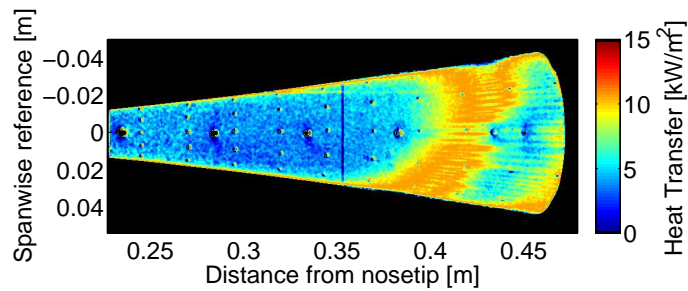

Figure 16. TSP image of compression cone without roughness elements, $p_0 = 148.7$ psia, Re $= 10.9 \times 10^6$/m, $T_0 = 430$ K.

The first array of epoxy dots had a height of 203 μm. Figure 17 shows a TSP image with the 203 μm epoxy dots at a unit Reynolds number of 10.9×10^6/m. It can be seen that the wave number around the circumference of the cone remains unchanged. The differences in the magnitude of heat transfer could not be compared to the cone without any roughness elements. The position of the calibration patch used for processing TSP images was changed from Figure 16 to Figure 17 resulting in differing TSP calibrations. Physically there are no obvious changes in the streak spacing.

The height of each epoxy dot was then increased to 305 μm with a width of 635 μm, corresponding to 4° of arc at their location on the cone. The TSP image shown in Figure 18 shows an obvious change in heating on the surface of the cone. Note that the apparent change in model shape is due to reduced levels of lighting on the upstream end of the cone. Analyzing the pressure transducer data, it was determined that the large second-mode waves were again present near 315 kHz, confirming that the roughness element interacted with the second-mode wave without acting as a boundary layer trip. It was determined that the wavenumber around the circumference of the cone had been reduced to 30, which coincides with the number of roughness elements. In order to determine if the streaks were physically connected to the roughness elements, the model was rolled in 5° increments and spanwise heat transfer profiles were produced from TSP images. Figure 19 shows the spanwise heat transfer profiles. It is evident that the streaks are caused by the
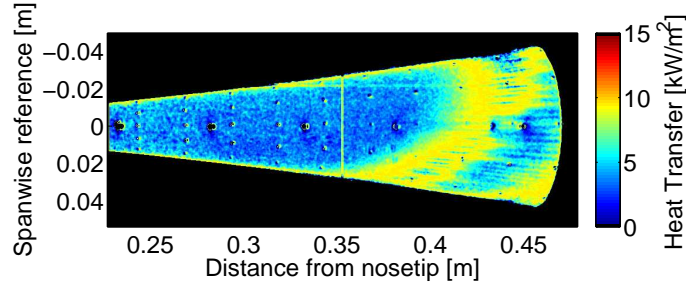
12

Figure 17. TSP image of compression cone with roughness elements 203 μm in height, $p_0 = 147.6$ psia, Re = 10.9×10^6/m, $T_0 = 427$ K.

roughness elements since they roll with the cone. Additional physical attributes of the streaks can be seen in the streamwise profiles. Each streak is actually made of two sub-streaks spaced approximately 4° apart, the same as the width of a roughness element. From the center of one streak pair to another is 12°, the distance between adjacent roughness elements.
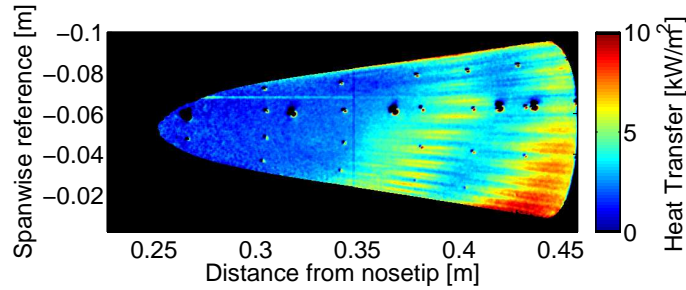

Figure 18. TSP image of compression cone with roughness elements 305 μm in height, $p_0 = 146.3$ psia, Re = 11.0×10^6/m, $T_0 = 429$ K.
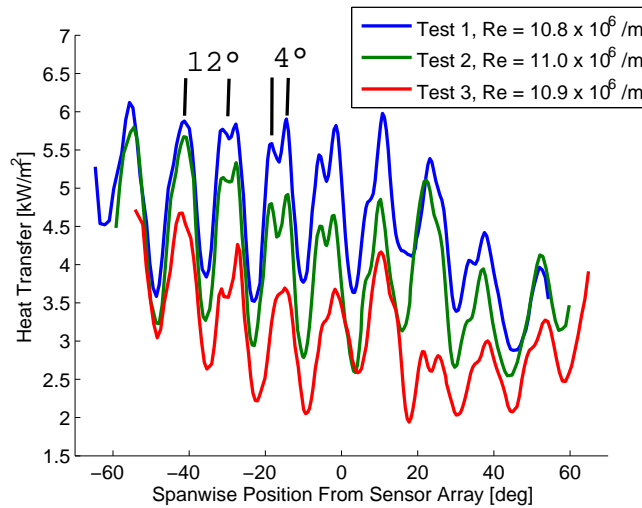

Figure 19. Spanwise heat transfer profiles with roughness elements 305 μm in height for three different tests with an average unit Reynolds number of 10.9×10^6/m.

13

Figure 20 is a TSP image near a stagnation pressure of 150 psia with the same flared cone using the smaller porthole windows available for use in the BAM6QT. With the smaller window, a different camera lens was used that resulted in greater image detail. This detail allowed for the investigation of the relationship between the initial increase in heating caused by the non-linear growth of second-mode waves and the secondary heating caused by the higher modes experiencing strong non-linear amplification. Taking spanwise heat transfer profiles as shown in Figure 20, the spacing of the steaks could be determined. Figure 21 shows that the center of the initial heating streaks is directly downstream of the roughness elements. However, the streaks from the second increase in heating are shifted by 6° in relation to the upstream streaks. The cause of this half-wavelength shift in streak location has not yet been determined. Computational comparisons are sought.
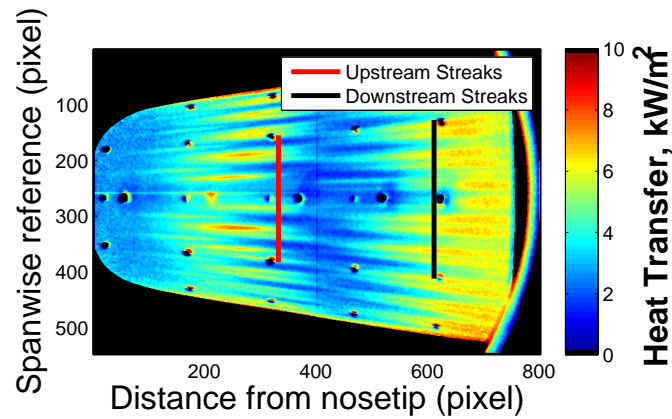

Figure 20. TSP image of compression cone with roughness elements 305 μm in height using porthole window in BAM6QT, $p_0 = 150.3$ **psia, Re = 11.0×10^6/m,** $T_0 = 426$ **K.**
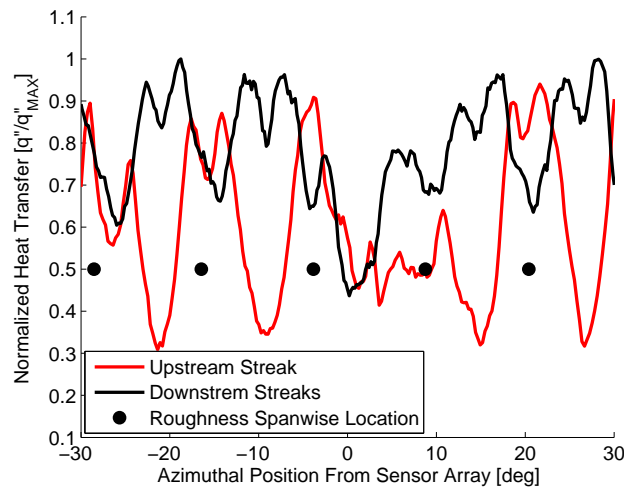
Figure 21. Spanwise heat transfer profiles with roughness elements 305 μm in height, $p_0 = 150.3$ **psia, Re = 11.0×10^6/m,** $T_0 = 426$ **K.**

14

V. Development of a Pulsed Jet Perturber for Generating Turbulent Spots in a Mach-6 Boundary Layer

Hypersonic vehicles undergoing boundary-layer transition are subject to high amplitude pressure fluctuations due to the intermittent passage of turbulent spots. The transitional region along hypersonic vehicles can extend over significant portions of the vehicle length.[13] It has been shown that the pressure fluctuations are higher within the transitional region than in the fully turbulent flow. However, the pressure fluctuation field within the transitional region of hypersonic vehicles is still poorly understood.

In order to accurately model the transitional pressure field, an intermittency model of turbulent spot transition could be used.[14] Turbulent spots are generated randomly in time and span at the transition onset location, and grow as they convect downstream. With knowledge of the growth rate of turbulent spots and the spot formation rate, the length of the transitional region can be determined. This can then be combined with knowledge of the pressure field underneath hypersonic turbulent spots to predict fluctuation amplitudes in transitional flow, similar to the model developed by Park and Lauchle for low-speed flat-plate flows.[14]

Casper measured some of the growth parameters of young turbulent spots in a hypersonic boundary layer using a pulsed glow perturber to disturb the nozzle-wall boundary layer in the BAM6QT.[15, 16] Casper was able to measure many spot characteristics, including the low-frequency footprint of turbulent spots and the leading and trailing edge convection rates. However, to develop a turbulent spot model of transition, growth rates must be measured for mature turbulent spots. A perturbation with a higher initial amplitude is required to ensure the development of mature turbulent spots in the BAM6QT. In order to accomplish this goal, a pulsed jet perturber was developed to inject a transverse jet into the BAM6QT's nozzle-wall boundary layer.

The basis of the pulsed jet perturber is a Parker Hannafin Corporation (Parker) #009-1669-900 pulse valve. Parker pulse valves are primarily used for spectroscopy experiments where pressurized specimens are injected into a vacuum chamber in order to cool the specimen via supersonic expansion. The valve provided an off-the-shelf component that was well suited to the pressure environments encountered during pressurization of the BAM6QT, as well as the low static pressures that occur during a tunnel run. A schematic of the valve is shown in Figure 22. The valve coil threads onto the valve body with a 1/2-28-UNEF thread. Internally, the valve consists of an armature with an internal load spring holding a poppet into place. The armature assembly is then inserted into the coil, and held into place with a buffer spring as the valve body is threaded onto the valve coil. Upon actuation of the valve, using a brief (70-80 μs) 320 V pulse, the armature is drawn back into the coil, and the poppet retracts to allow flow through a 0.039-inch exit-orifice on the stock valve. The total travel of the valve is on the order of 0.003-0.005 inches. The valve injects the jet into the nozzle-wall boundary layer through a 0.039-inch-diameter orifice located at $z = 1.924$ m, where z denotes the distance downstream of the throat. In order to prepare the valve for use, the valve had to be aligned. The valve alignment was the one dimensional process of threading the coil onto the body to alter the position of the internal valve components.

The valve was used to inject a jet into the nozzle-wall boundary layer at the Re $= 11.4 \times 10^6$/m. Pressure histories were measured using a streamwise array of Kulite XCQ-062-15A A-screen pressure transducers. Figure 23 shows the response of the stock valve with a valve stagnation pressure of 80 psig. Each pressure trace is normalized by the theoretical freestream static pressure and vertically offset proportionally to its distance downstream. The spectra indicate a fully turbulent perturbation at all measurement locations. This is a large step forward in generating mature turbulent spots in the BAM6QT. However, the perturbation duration is almost 2 ms, which at the freestream velocities in the BAM6QT would result in perturbations well over 1 m in length. At this length, the perturbations are long enough that they are likely a turbulent wake caused by a quasi-steady flow field, as opposed to true turbulent spots.

As familiarity was gained with the pulse valve system, the perturbation duration was reduced. Figure 24 shows the shortest duration perturbation generated using the pulse valve. The perturbation has a duration of approximately 700 μs at $z = 2.831$ m. The large reduction in duration was due to the elimination of a low voltage portion of the signal that drives the valve. This low voltage pulse was designed to hold the valve open for additional time without overheating the valve coil. The electronics that drove the valve were
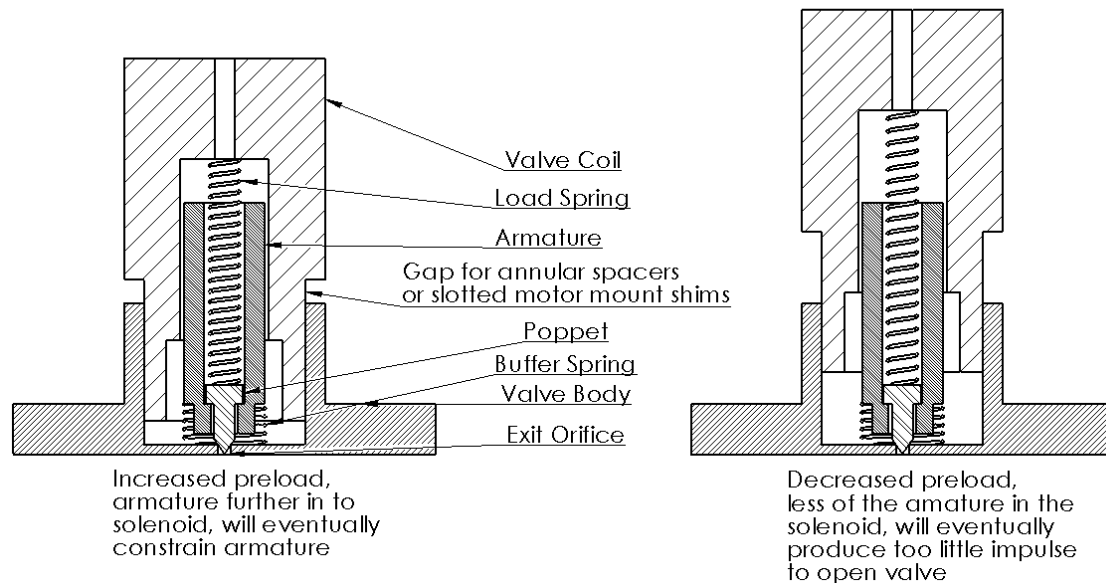
15

Figure 22. Cutaway schematic of the internals of the Parker pulse valve.

physically modified to remove this pulse. Additional reduction in perturbation duration was likely due to improved valve alignment.

The current valve design causes a large difficulty in accurately aligning the valve, as well as maintaining the valve alignment once it has been set, as the valve is very sensitive to slight adjustments. A new method for aligning the valve is under development using a high precision micrometer head. Improvements are being sought to reduce the duration of the blow-down portion of the perturbation. Further detail on this project can be found in Abney's Master's thesis.[17]

VI.   Measurements of Possible Entropy-Layer Instabilities off the Surface of Cone-Ogive-Cylinder Configurations

Predicting the onset of boundary layer transition is critical in hypersonic flight. The three to eight-fold increase in heat transfer with its added thermal protection requirements and the significant change in body forces necessitate accurate transition prediction. A better understanding of the underlying mechanisms that cause transition is necessary to improve transition prediction methods. In addition to boundary-layer instabilities, entropy-layer instabilities are of particular interest in the design of blunt reentry vehicles and vehicles at high angles of attack.

Experimental measurements of apparent entropy-layer instabilities are being conducted using slender cone-ogive-cylinder models in the BAM6QT. Measurements using robust surface sensors have been made at various axial locations on the surface of the model. These measurements are compared with pitot transducer and hot-wire measurements made at various distances from the model. The goal of these measurements is to help understand the effect that entropy-layer instabilities have on the stability of a laminar boundary layer.

A.   Introduction

In supersonic flow, variations in the strength of a shock along its length create large temperature and velocity gradients normal to the streamlines. These affect the downstream flow characteristics close to the body.[18]
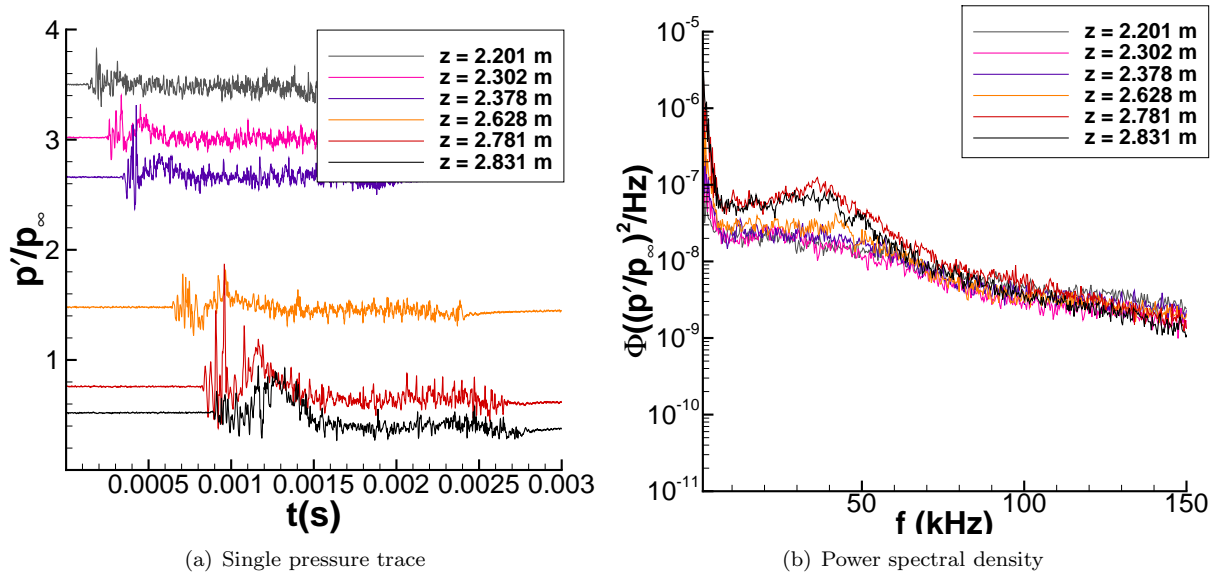
16

(a) Single pressure trace

(b) Power spectral density

Figure 23. Perturbation generated by the stock pulse valve. Re $= 11.4{\times}10^6$/m, $p_{0v} = 80$ psig.

(a) Single pressure trace

(b) Power spectral density

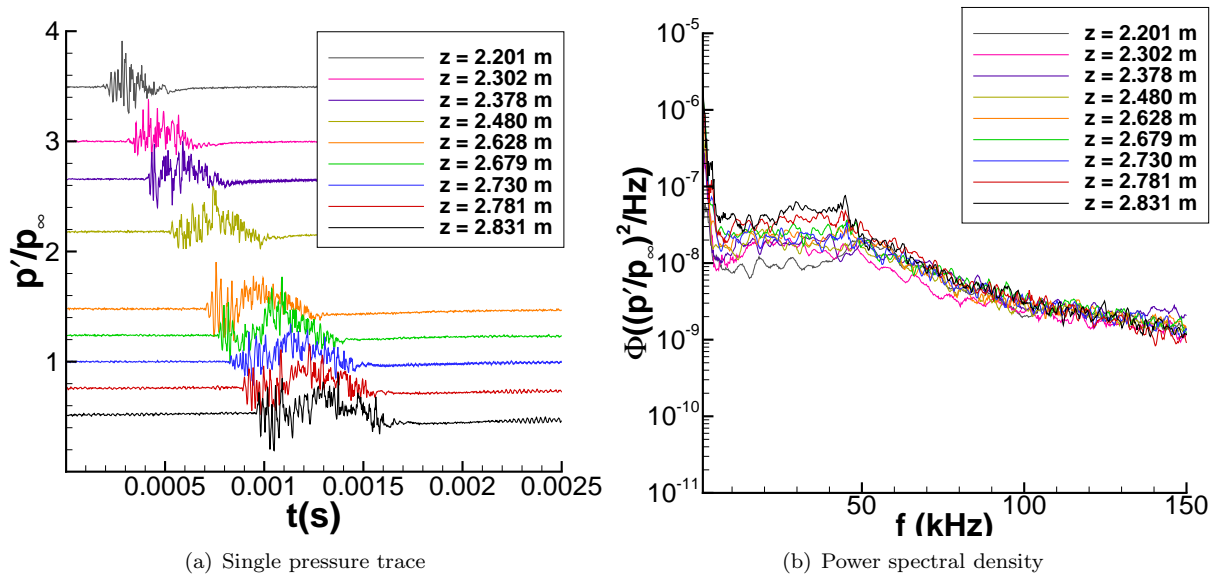**Figure 24. Perturbation generated by the stock pulse valve using the modified AAE electronics. Re $= 11.4{\times}10^6$/m, $p_{0v} = 80$ psig.**

17

These entropy gradients are particularly important for blunt objects that have large strength variations along the shock.[19]

Previous experiments have shown that the entropy layer affects transition location, demonstrating its effect on the critical Reynolds number. They have shown that a small amount of bluntness on a cone increases the distance to the transition location. Then, as the nose bluntness is increased further, there comes a point where the transition location moves forward on the frustum. This transition reversal is not unique to a specific facility[20] and is believed to be an effect of the interaction between the entropy and boundary layers.[21–23] A similar transition reversal due to bluntness was shown by Lysenko to occur on flat plates.[24]

Numerical studies have also investigated entropy-layer instabilities and their role in transition reversal[25].[26] A study by Reshotko and Khan predicted separate instabilities in the boundary layer and the entropy layer. Their computations predicted entropy-layer instabilities that were similar to first-mode instabilities for a supersonic boundary layer.[27] In another study, Federov and Tumin hypothesized that the inviscid entropy layer's interaction with the viscous boundary layer may cause transition reversal by changing the overall stability characteristics and the resultant transition locus.[28]

Stetson et al. measured low frequency (under 100kHz), inviscid instabilities inside the entropy layer using hot wire anemometry. They followed the instability downstream until it was swallowed up in the boundary layer. They discovered that the entropy-layer disturbances grew slowly outside the boundary layer, diminished slightly as they entered the boundary layer, and then proceeded to grow rapidly inside the boundary layer.[25] Lysenko was also able to use hot wires to measure the existence of inviscid, entropy-layer instabilities above a flat plate. He also tried to measure the pressure fluctuations using surface pressure transducers but was unsuccessful due to the low signal levels.[24]

Previous experimental measurements were made in the BAM6QT with a 30-degree cone-ogive-cylinder model using Kulite pressure transducers on the surface and in a pitot configuration off the surface. The data from these preliminary measurements showed evidence of an entropy-layer instability outside the predicted boundary layer that appears to approach the model as it proceeds axially.[30]

This study is being continued with additional measurements of the entropy-layer instability in order to better understand the physics behind these instabilities. Hot wire anemometry is now being used off the model surface in order to get more precise measurements of the instability location and magnitude.

B.   Computational Setup

The mean flow was calculated using Stability and Transition Analysis for Hypersonic Boundary Layers (STABL). STABL is a two-dimensional/axisymmetric, Navier-Stokes solver that uses implicit Data-Parallel Line Relaxation (DPLR). Computations were made for each design under BAM6QT operating conditions. Stability analysis was also completed using PSE-Chem which solves the parabolized stability equations and predicts the N factor for each instability mode in the boundary layer.[31, 32] Although STABL can compute first and second-mode instabilities, it cannot at present compute entropy-layer instabilities.

C.   Experimental Setup

The cone-ogive-cylinder design consists of a cone that tapers into an ogive-cylinder. Initial measurements were taken with surface and pitot pressure transducers on a 30-degree model. Because the initial measurements taken showed evidence of an entropy-layer instability a new model was built to vary the shock curvature, and thereby affect the entropy layer.

The new cone-ogive-cylinder model consists of a long cylindrical body with the same 5-cm diameter as the original model but with detachable 25, 30, 35, and 40-degree cone-ogive nosetips. The profiles of these nosetips are shown in Figure 25. In order to compare with previous results, when the new model has the 30-degree nosetip installed, it has the same dimensions as the original model. This new model allows for measurements of entropy-layer instabilities over a range of shock curvatures. A photo of the cylinder and its interchangeable nosetips is shown in Figure 26.
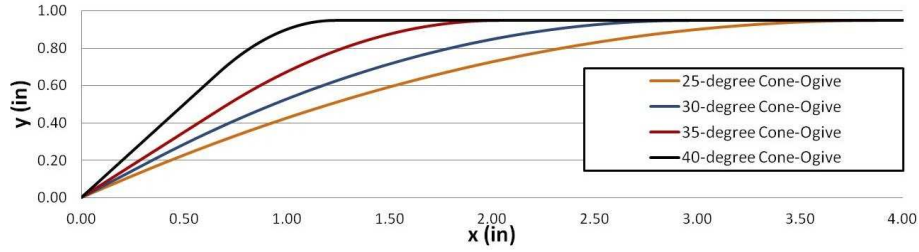
18

Figure 25. Profiles of the four cone-ogive-cylinder leading-edge configurations.

The cone-ogive-cylinder model and the interchangeable nosetips were fabricated in the Purdue machine shop. They were made of 6061-T6 aluminum and when put together, the cone-ogive-cylinder has a total length of 94 cm.

Figure 26. Picture of cone-ogive-cylinder model with interchangeable cone-ogive portions.

The sketch of the cone-ogive-cylinder in Figure 27 shows the pressure transducer port locations for inserting Kulite pressure transducers in the model surface. They have been machined in the cone-ogive-cylinder at 8 axial locations ranging from 0.52 to 0.86 meters. One additional port was machined at the 0.62-meter location with the two holes separated by 0.25 centimeters, measured from the port centers. (The original model had surface pressure transducers installed from 0.58 to 0.91 meters).
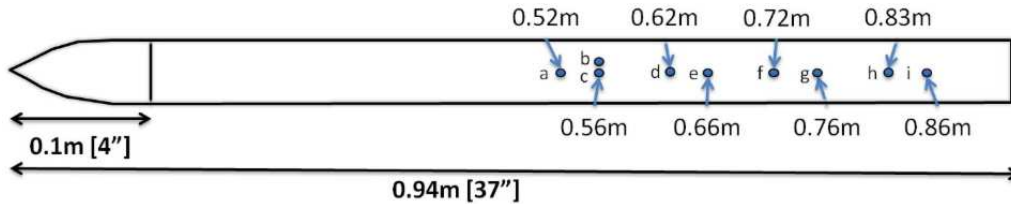

Figure 27. Sketch of the cone-ogive-cylinder model with surface sensor locations labeled.

Hot-wire anemometers were used to measure disturbances off the surface of the model. Axial positioning of the hot-wire apparatus can be made between runs, and a traversing system with a stepping motor allows for vertical displacement during the run. A close-up picture of one of the hot-wire probes used is shown in Figure 28. These hot-wire probes were built by Jim Younts of the Purdue machine shop. He also replaced hot-wire filaments when they broke during usage.

D. Computational Results

Computations of the mean flow over the 25, 30, and 35-degree configurations were performed. The angular momentum was calculated at several axial locations and these profiles are shown in Figure 29. The angular momentum plots for each configuration show generalized inflection point starting at various distances downstream. The inflection points are shown by knees in the profile curves above the predicted boundary layer.

19

Figure 28. Picture of a hot-wire probe used in the BAM6QT.

The inflection point is one indicator of the stability of the entropy layer. Where there is a local maximum, there is the possibility of an instability growth.[33, 34]
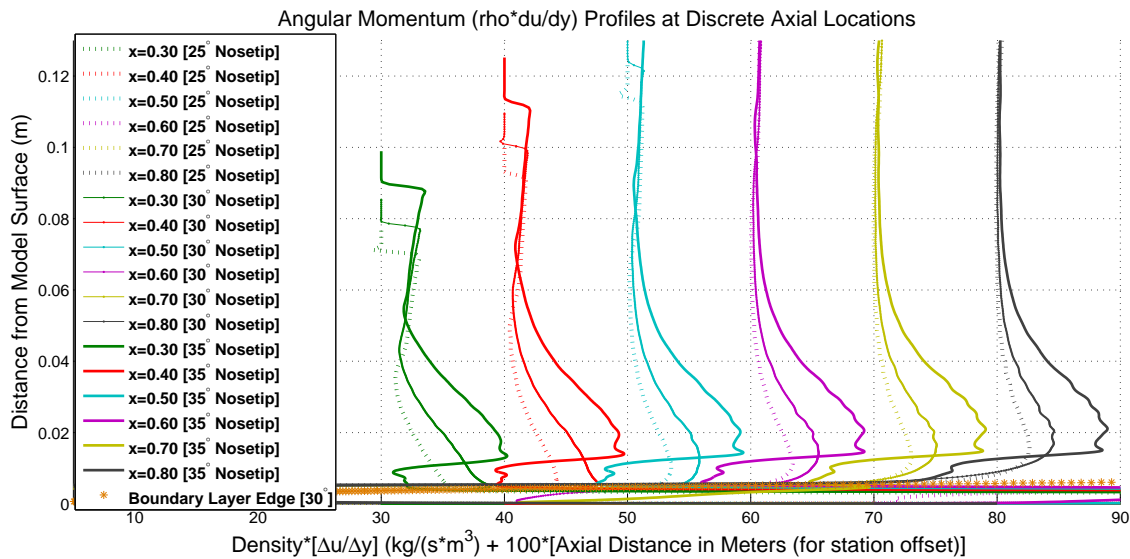

Figure 29. Calculated angular momentum profiles for the 25, 30, and 35 degree cone-ogive-cylinder configurations.

E. Experimental Results

1. Surface Measurements

Figure 30 shows the power spectra obtained from measurements at several axial locations on the surface of the 30-degree cone-ogive-cylinder. At each measured location, an instability is measured on the model surface. The spectra shows disturbance magnitude peaks at around 25 and 35 kHz.

Between the first two measurement locations (58 and 61 cm), the 25-kHz peak magnitude increases. The next two locations (71 and 81 cm) show the magnitude of the peak leveling out and then decreasing significantly. Then the instability grows substantially before being measured at the last sensor at 91 cm.

The 35-kHz peak follows a similar trend showing an initial instability growth, followed by a magnitude decrease, and then a rapid growth. The data for an individual run with the 30-degree cone-ogive-cylinder
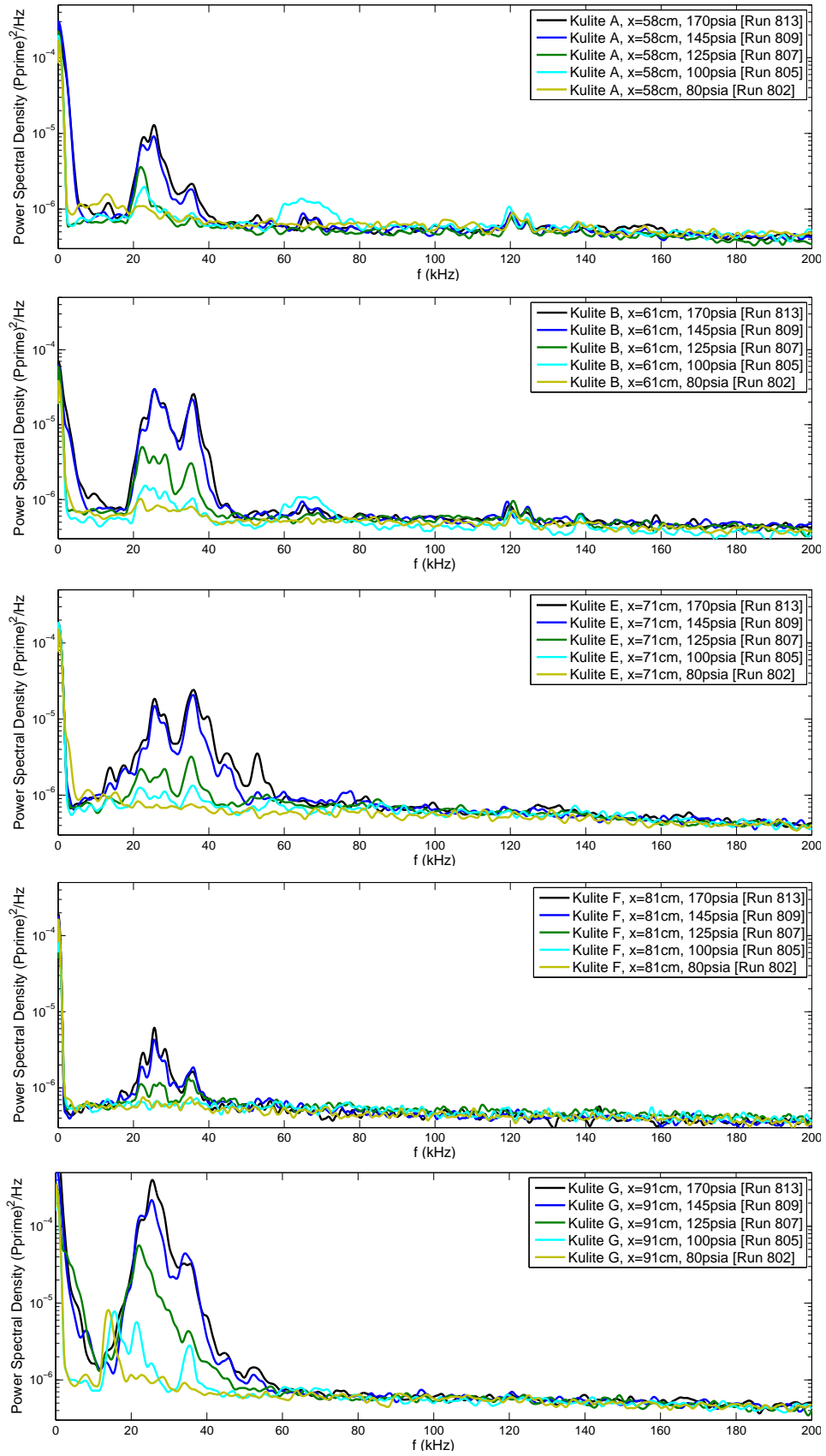
20

Figure 30. Power Spectra of surface measurements at increasing axial locations on the 30-degree cone-ogive-cylinder. These spectra show how the measured instability magnitude increases, then decreases, and finally increases rapidly.

at a total pressure of 145 psia is shown in Figure 31 with the spectra for each axial location offset on the y-axis.
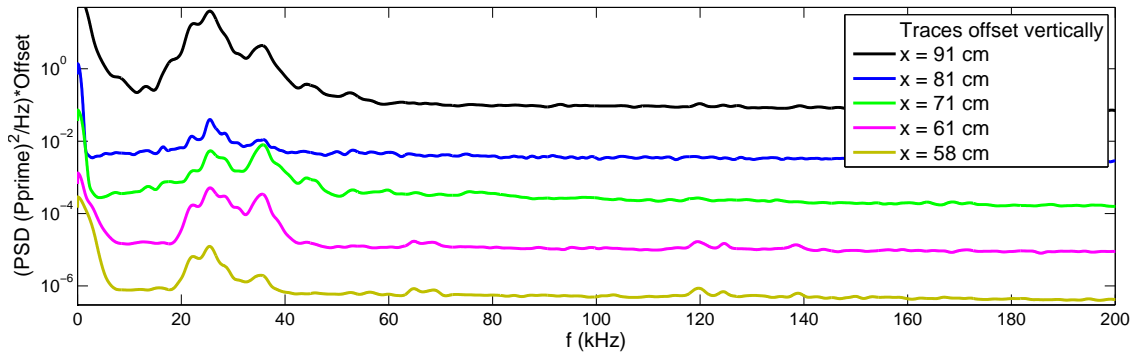

Figure 31. Power spectra showing decrease and subsequent increase in disturbance magnitude with axial progression on the 30-degree cone-ogive-cylinder [Run 809, p_0=145psia].

This decrease of instability magnitude may be due to the stabilizing effect of the entropy-layer being swallowed by the boundary layer as described by Stetson.[25] However, additional measurements and computations are needed to confirm whether that is the case or whether it is due to some other non-linear interaction.

The 35-degree cone-ogive-cylinder configuration shows a similar instability growth and stabilization trend, but the stabilization begins further forward on the model. The power spectra showing the decrease and subsequent increase in instability magnitude measured on the 35-degree cone-ogive-cylinder configuration is shown in Figure 32 with the spectra for each axial location offset on the y-axis. The spectra shows a 35 kHz instability that grows initially, but then starts to decay after the surface sensor at 56 cm. The disturbance magnitude then increases significantly between 72 and 86 cm.
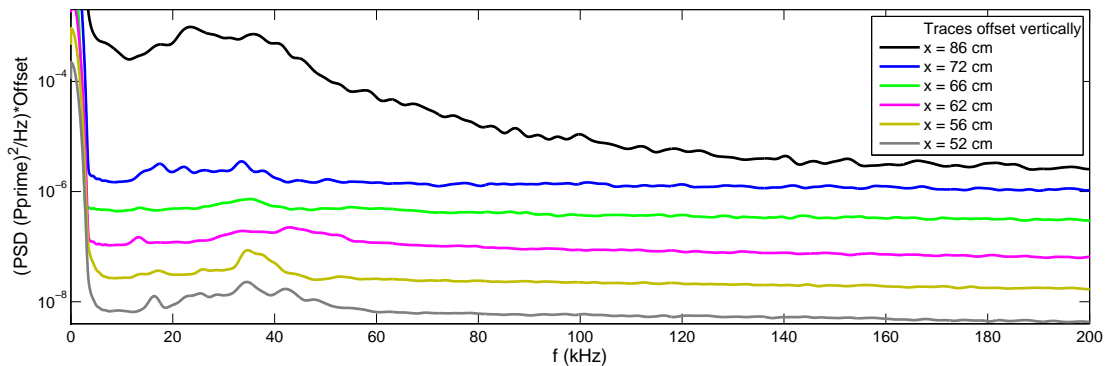

Figure 32. Power spectra showing decrease and subsequent increase in disturbance magnitude with axial progression on the 35-degree cone-ogive-cylinder [Run 1219, p_0=125psia].

The nosetip affects both the magnitude and frequency of the measured instabilities. The power spectra for the 25, 30, and 35-degree cone-ogive-cylinder configurations at 62 cm is shown in Figure 33. These spectra show an obvious increase in instability magnitude with increasing nosetip angle. The frequency of the peak instabilities also decreases slightly with increasing nosetip angle.

22
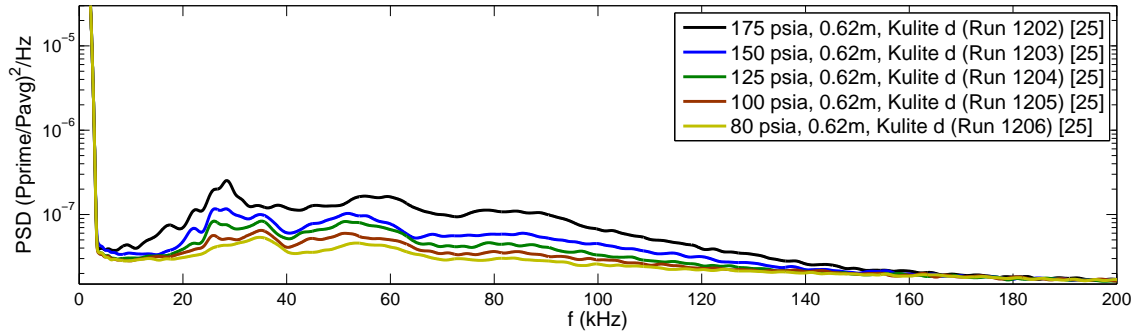
(a) Surface measurements on 25-degree configuration at x=62cm.
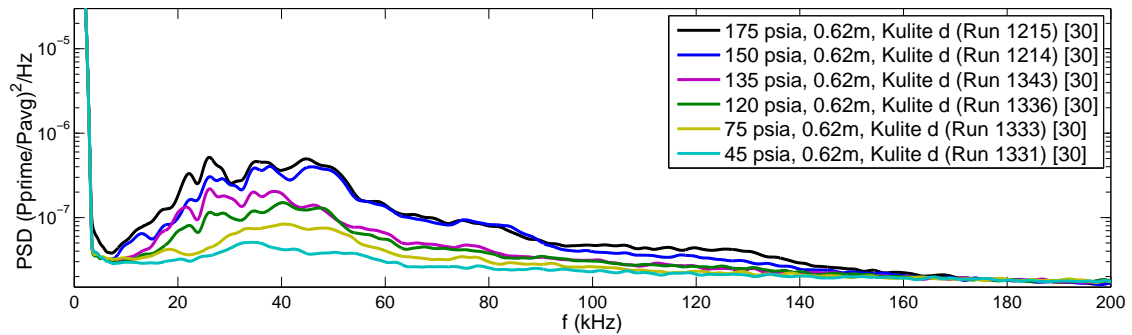
(b) Surface measurements on 30-degree configuration at x=62cm.
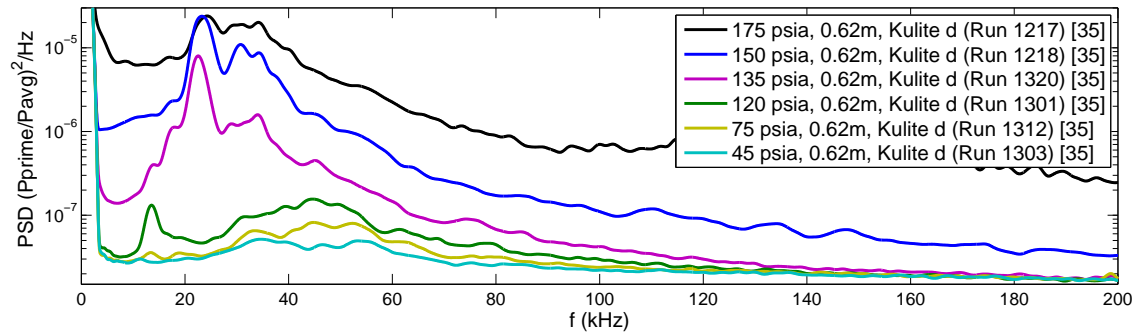
(c) Surface measurements on 35-degree configuration at x=62cm.

Figure 33. Power Spectra of surface measurements at 62cm for 25, 30, and 35-degree cone-ogive-cylinder configurations.
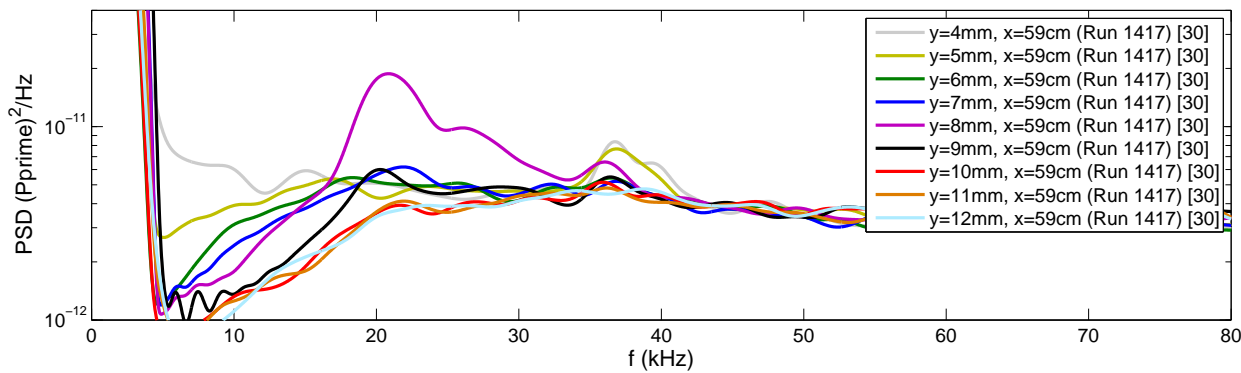
2. Hot-wire Measurements

Previous pitot measurements had shown an instability outside the predicted boundary layer.[30] The goal of the hot-wire measurements was to get clearer measurements of the location and magnitude of these instabilities. The best hot-wire measurements were taken at three axial locations above the 30-degree cone-ogive-cylinder and are shown in Figure 34. The maximum instability magnitude at 56 cm is shown in Figure 34(a) by the red line. At this axial location, it is about 10 mm above the surface of the model. This is about twice the distance from the model as the predicted 5 mm boundary layer thickness.

Further downstream, the magnitude of the measured instability increases and the distance from the model decreases. At 59 cm, the instability is only about 8 mm from the model surface as shown by the purple line in Figure 34(b). Then at 62 cm, the location of maximum disturbance is only 6 mm as shown by the green line in Figure 34(c), very close to the predicted boundary layer.

Planned hot-wire measurements at additional axial locations and using different nosetips will give a better understanding of the progression of these instabilities, including how the instability is affected by nosetip angle. It would be very desirable to have numerical calculations to compare with these measurements.
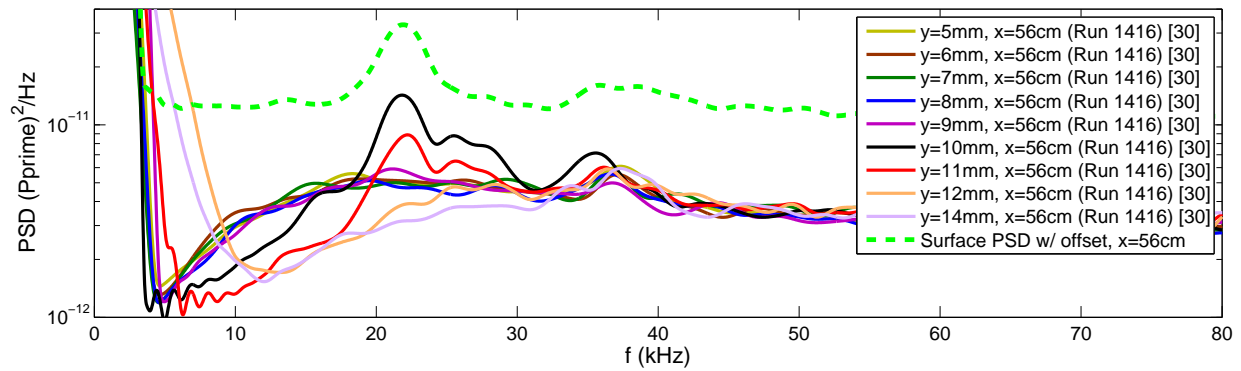
(a) Hot-wire PSD above the 30-degree cone-ogive-cylinder at at x=0.56m, p_0=120psia.

(b) Hot-wire PSD above the 30-degree cone-ogive-cylinder at at x=0.59m, p_0=120psia.
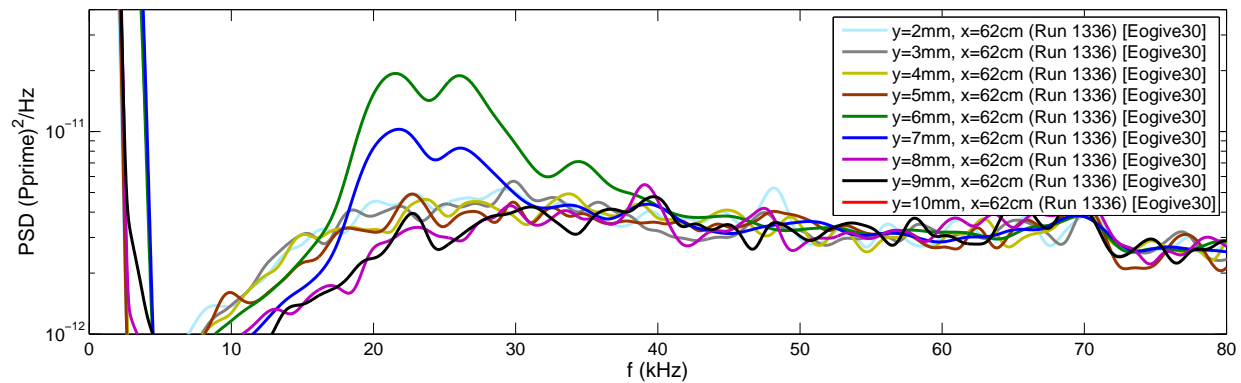
(c) Hot-wire PSD above the 30-degree cone-ogive-cylinder at at x=0.62m, p_0=120psia.

Figure 34. Power spectra of hot-wire measurements off the surface of the 30-degree cone-ogive-cylinder at three axial locations.

VII.   Conclusions

1. Three different highly swept fins were tested. Temperature-sensitive paint was used to visualize the vortices that form near the corner junction of the fin with the cone body. In addition, PCB pressure transducers were used to measure fluctuations inside the shock and near where the shock impinges on the cone body.

2. Roughness elements were used to successfully control the streaks of heating caused by second-mode wave saturation and breakdown on a flared cone. It was observed that each streak is composed of two sub-streaks. The spacing between the streaks correlated to the spacing of the discrete roughness elements.

3. Experiments were performed looking at the effect of roughness on the stationary and travelling cross-flow waves on a cone at angle of attack. When roughness patches were added to the cone, the stationary waves increased in amplitude. As the stationary wave amplitudes increased, the travelling wave amplitudes were subsequently damped. The interaction between the travelling and stationary waves is poorly understood and requires further investigation. It was also found that as the model wall temperature increased, the amplitude of the travelling waves also increased.

4. A pulsed jet perturber was used to inject a jet into the nozzle-wall boundary layer. The perturber was improved to create shorter pulses to generate turbulent bursts. Aligning the valve proved to be a non-trivial factor, leading to the design and fabrication of a new test apparatus. Future testing will involve the new design to determine if shorter and more repeatable bursts can be created.

5. Initial measurements of entropy-layer instabilities have been made using surface pressure transducers and hot-wire anemometers in the BAM6QT. A long cone-ogive-cylinder model with interchangeable nosetips with a range of leading-edge half-cone angles has been used to vary the entropy layer. Surface measurements show an instability magnitude that increases, then decreases, and eventually increases rapidly. This may be due to the entropy-layer entering the boundary layer. Hot-wire measurements show the instability approaches the model as it moves downstream supporting this theory. Surface and hot-wire measurements also show that the frequency and magnitude of the measured instability is dependent on the nosetip used. The higher nosetip angles have lower frequency and higher magnitude instabilities.

VIII.   Acknowledgements

References

[1]Hummel, D., "Axial Flow in Corners at Supersonic and Hypersonic Speeds." *AGARD Report No. 764, Special Course on Three-Dimensional Supersonic/Hypersonic Flows Including Separation*, January 1990, pp. 5–2 to 5–37.

[2]Casper, K. M., *Hypersonic Wind-Tunnel Measurements of Boundary-Layer Pressure Fluctuations*, Master's thesis, Department of Aeronautics and Astronautics, Purdue University, West Lafayette, IN, 2009.

[3]Saric, W., Reed, H., and White, E., "Stability and Transition of Three-Dimensional Boundary Layers," *Annual Review of Fluid Mechanics*, Vol. 35, 2003, pp. 413–440.

[4]Deyhle, H. and Bippes, H., "Disturbance Growth in an Unstable Three-Dimensional Boundary Layer and its Dependence on Environmental Conditions," *Journal of Fluid Mechanics*, Vol. 316, December 1996, pp. 73–113.

[5]Saric, W. S., Jr., R. B. C., and Reibert, M. S., "Nonlinear Stability and Transition in 3-D Boundary Layers," *Meccanica*, Vol. 33, 1998, pp. 469–487.

[6]Corke, T., Matlis, E., Schuele, C.-Y., Wilkinson, S., Owens, L., and Balakumar, P., "Control of Stationary Cross-flow Modes Using Patterned Roughness at Mach 3.5," *7th IUTAM Symposium on Laminar-Turbulent Transition*, 2010, pp. 123–128.

[7]Schuele, C. Y., *Control of Stationary Cross-Flow Modes in a Mach 3.5 Boundary Layer Using Patterned Passive and Active Roughness*, Ph.D. thesis, University of Notre Dame, South Bend, Indiana, December 2011.

[8]Borg, M. P., Kimmel, R., and Stanfield, S., "Crossflow Instability for HIFiRE-5 in a Quiet Hypersonc Wind Tunnel," AIAA Paper 2012-2821, June 2012.

[9]Chou, A., Ward, C. A. C., Letterman, L. E., Luersen, R. P. K., Borg, M. P., and Schneider, S. P., "Transition Research with Temperature-Sensitive Paints in the Boeing/AFOSR Mach-6 Quiet Tunnel," AIAA Paper 2011-3872, June 2011.

[10]Sivasubrahmanian, J. and Fasel, H., "Numerical Investigation of Laminar-Turbulent Transition in a Cone Boundary Layer at Mach 6," AIAA Paper 2011-3562, June 2011.

[11]Ward, C., Wheaton, B., Chou, A., Gilbert, P., Steen, L., and Schneider, S., "Boundary-Layer Transition Measurements in a Mach-6 Quiet Tunnel," AIAA Paper 2010-4721, June 2010.

[12]Luersen, R. P., *Techniques for Application of Roughness For Manipulation of Second-Mode Waves on a Flared Cone at Mach 6*, Master's thesis, Purdue University School of Aeronautics and Astronautics, December 2012.

[13]Wright, R. and Zoby, E., "Flight Boundary Layer Transition Measurements on a Slender Cone at Mach 20," AIAA Paper 77-719, June 1977.

[14]Park, S. and Lauchle, G. C., "Wall pressure fluctuation spectra due to boundary-layer transition," *Journal of Sound and Vibration*, Vol. 319, 2009, pp. 1067–1082.

[15]Casper, K., Beresh, S., and Schneider, S., "Spanwise Growth of the Turbulent Spot Pressure-Fluctuation Field in a Hypersonic Boundary Layer," AIAA Paper 2011-3873, June 2011.

[16]Casper, K. M., *Pressure Fluctuations Beneath Instability Wave Packets and Turbulent Spots in a Hypersonic Boundary Layer*, Ph.D. thesis, Purdue University School of Aeronautics and Astronautics, August 2012.

[17]Abney, A. D., *A Pulsed Jet for Generation of Turbulent Spots in a Mach 6 Boundary Layer*, Master's thesis, Purdue University School of Aeronautics and Astronautics, December 2013.

[18]Anderson, J. D., *Modern Compressible Flow with Historical Perspective*, Vol. 1, The McGraw-Hill Companies, Inc., New York, New York, 3rd ed., 2003.

[19]Anderson, J. D., *Hypersonic and High-Temperature Gas Dynamics*, Vol. 1, American Institute of Aeronautics and Astronautics, Inc., Reston, Virginia, 1st ed., 1989.

[20]Stetson, K. F., "Nosetip Bluntness Effects on Cone Frustum Boundary Layer Transition in Hypersonic Flow," *16th Fluid and Plasma Dynamics Conference*, AIAA 83-1763, Danvers, MA, July 1983.

[21]Stetson, K. F. and Rushton, G. H., "Shock Tunnel Investigation of Boundary-Layer Transition at M = 5.5," *AIAA Journal*, Vol. 5, No. 5, 1967, pp. 899–906.

[22]Softley, E. J., Graber, B. C., and Zempel, R. E., "Experimental Observation of Transition of the Hypersonic Boundary Layer," *AIAA Journal*, Vol. 7, No. 2, 1969, pp. 257–263.

[23]Softley, E. J., "Boundary Layer Transition on Hypersonic Blunt, Slender Cones," *AIAA Fluid and Plasma Dynamics Conference*, AIAA 69-705, San Francisco, CA, June 1969.

[24]Lysenko, V. I., "Influence of the Entropy Layer on the Stability of a Supersonic Shock Layer and Transition of the Laminar Boundary Layer to Turbulence," *Journal of Applied Mechanics and Technical Physics, Translated from Zhurnal Prikladnoi Mekhaniki i Tekhnicheskoi Fiziki*, Vol. 31, No. 6, 1990, pp. 868–873.

[25]Stetson, K. F., Thompson, E. R., Donaldson, J. C., and Siler, L. G., "Laminar Boundary Layer Stability Experiments on a Cone at Mach 8, Part 2: Blunt Cone," *22nd AIAA Aerospace Sciences Meeting and Exhibit*, AIAA 84-0006, Reno, NV, January 1984.

[26]Malik, M., Spall, R. E., and Chang, C.-L., "Effect of Nose Bluntness on Boundary Layer Stability and Transition," *28th AIAA Aerospace Sciences Meeting*, AIAA 90-0112, Reno, NV, January 1990.

[27]Reshotko, E. and Khan, M. M. S., "Stability of the Laminar Boundary Layer on a Blunted Plate in Supersonic Flow," *Laminar-Turbulent Transition, IUTAM Symposium*, edited by R. Eppler and H. Fasel, Springer-Verlag, Stuttgart, Germany, September 1980, pp. 186–200.

[28]Fedorov, A. and Tumin, A., "Evolution of Disturbances in Entropy Layer on Blunted Plate in Supersonic Flow," *AIAA Journal*, Vol. 42, No. 1, 2004, pp. 89–94.

[29]Chang, S. C., Wang, X. Y., and Chow, C., "The Method of Space-Time Conservation Element and Solution Element: A New High-Resolution and Genuinely Multidimensional Paradigm for Solving Conservation Laws," *Journal of Computational Physics*, Vol. 156, No. 1, 1999, pp. 89–136.

[30]Ward, C. A. C., Greenwood, R. T., Abney, A. D., and Schneider, S. P., "Boundary-Layer Transition Experiments in a Hypersonic Quiet Wind Tunnel," *AIAA 43rd Fluid Dynamics Conference*, AIAA 2013-2738, San Diego, CA, June 2013.

[31]Johnson, H. B., *Stability and Transition Analysis for Hypersonic Boundary Layers Program Reference*, University of Minnesota, 2010.

[32]Johnson, H. B. and Candler, G. V., "Hypersonic Boundary Layer Stability Analysis Using PSE-Chem," *35th Fluid Dynamics Conference*, AIAA 2005-5023, Toronto, Canada, June 2005.

[33]Reshotko, E., "Boundary Layer Instability, Transition and Control," *32nd Aerospace Sciences Meeting and Exhibit*, AIAA 94-0001, Reno, NV, January 1994.

[34]Lees, L. and Lin, C. C., "Investigation of the Stability of the Laminar Boundary Layer in a Compressible Fluid," Tech. Rep. Technical Note No. 1115, NACA, 1946.